A Complementary Experimental and Theoretical Approach for Probing the Surface Functionalization of ZnO with Molecular Catalyst Linkers

Shravan R. Kousik, Helena Solodenko, Azade YazdanYar, Manuel Kirchhof, Peter Schützendübe, Gunther Richter, Sabine Laschat, Maria Fyta, Guido Schmitz, Joachim Bill, and Petia Atanasova*

The application of ZnO materials as solid-state supports for molecular heterogeneous catalysis is contingent on the functionalization of the ZnO surface with stable self-assembled monolayers (SAMs) of catalyst linker molecules. Herein, experimental and theoretical methods are used to study SAMs of azide-terminated molecular catalyst linkers with two different anchor groups (silane and thiol) on poly and monocrystalline (0001, $10\bar{1}0$) ZnO surfaces. Angle-resolved and temperature-dependent X-ray photoelectron spectroscopy (XPS) is used to study SAM binding modes, thermal stabilities, and coverages. The binding strengths and atomistic ordering of the SAMs are determined via atom-probe tomography (APT). Density functional theory (DFT) and ab initio molecular dynamics (AIMD) calculations provide insights on the influence of the ZnO surface polarity on the interaction affinity and conformational behavior of the SAMs. The investigations show that SAMs based on 3-azidopropyltriethoxysilane possess a higher binding strength and thermal stability than the corresponding thiol. SAM surface coverage is strongly influenced by the surface polarity of ZnO, and the highest coverage is observed on the polycrystalline surface. To demonstrate the applicability of linker-modified polycrystalline ZnO as a catalyst support, a chiral Rh diene complex is immobilized on the azide-terminal of the SAM and its coverage is evaluated via XPS.

1. Introduction

The high stereo and regioselectivities of enzymes can be attributed to their spatially confined catalytic active sites.[1,2] However, enzymes are generally incompatible with high temperatures and harsh organic solvents. To overcome the limitations of enzymatic catalysis, efforts have been directed toward the fabrication of highly selective and thermochemically stable solid-state catalysts,[3] usually achieved via the immobilization of well-defined molecular catalysts on mesoporous scaffolds such as metal–organic frameworks (MOFs), covalent organic frameworks (COFs), or oxide-based materials.[4–8] Among these, the use of oxide-based materials as solid-state support materials for molecular heterogeneous catalysis under confinement has gained considerable attention in recent years.[4,8–10] This can primarily be attributed to the diverse surface functionalities and porosities that can be achieved by exerting control over the composition

S. R. Kousik, J. Bill, P. Atanasova
Institute for Materials Science
University of Stuttgart
Heisenbergstraße 3, 70569 Stuttgart, Germany
E-mail: atanasova@imw.uni-stuttgart.de

H. Solodenko, G. Schmitz
Chair of Material Physics
Institute for Materials Science
University of Stuttgart
Heisenbergstraße 3, 70569 Stuttgart, Germany

A. YazdanYar, M. Fyta
Institute for Computational Physics
University of Stuttgart
Allmandring 3, 70569 Stuttgart, Germany

M. Kirchhof, S. Laschat
Institute of Organic Chemistry
University of Stuttgart
Pfaffenwaldring 55, 70569 Stuttgart, Germany

P. Schützendübe, G. Richter
Max Planck Institute for Intelligent Systems
Heisenbergstraße 3, 70569 Stuttgart, Germany

M. Fyta
Computational Biotechnology
RWTH Aachen University
Worringerweg 3, 52074 Aachen, Germany

and morphology of the oxide material.[11] Of the many oxide materials that have been considered for catalyst support applications, ZnO is of particular interest owing to its demonstrably high chemical and thermal stabilities.[12–14]

However, in order to operationalize ZnO materials as solid-state supports for molecular heterogeneous catalysis, their surfaces need to be modified by the incorporation of catalyst linker molecules with tailored functional groups.[15–17] Specifically, the support surface is functionalized with self-assembled monolayers (SAMs) of bifunctional catalyst linkers. These linkers contain two terminals: an anchor group (such as silane, thiol or phosphonate) that grafts onto the oxide surface, and a functional group (such as azide or isocyanide) that provides sites for the immobilization of the molecular catalyst.[9,18] The polarity of the ZnO surface, the anchor group and alkyl chain length of the linker are important determinants of the stability and packing density of the SAMs.[19–22] Owing to the well-established chemistry of alkanethiol monolayers on Au surfaces,[23–25] organothiols have been frequently used as anchor groups for the surface modification of ZnO as well.[19,26–34] While the self-assembly of silane-containing SAMs on SiO_2 is well-documented, it has not been extensively applied to ZnO.[35–40] This can be attributed to variations in the surface hydroxyl concentration on different oxide surfaces, a parameter that has a strong influence on the efficiency of silane immobilization.[41]

Despite the existence of studies on molecular adsorption on ZnO surfaces,[20,31,32,37,42–46] the influence of the surface polarity of ZnO and the anchor group on the binding modes, stability and coverage of SAMs remains unclear. Reports in this direction are usually restricted to the adsorption of long chain molecules (12–18 carbon atoms) on monocrystalline ZnO surfaces.[47,48] It is also important to note that macroscopic assemblies of ZnO are generally polycrystalline, an aspect that has been largely overlooked in previous studies. In a seminal work, Perkins showed that the thermal stability of *n*-hexanethiol SAMs on polycrystalline ZnO surfaces was lower than that of their phosphonic acid counterparts.[21] Notwithstanding, the interaction of short chain (3–4 carbon atoms) bifunctional linkers with ZnO surfaces continues to be poorly understood. In a preliminary effort, we studied the thermal stability of molecularly adsorbed 3-azidopropylthiol SAMs on (10$\bar{1}$0) ZnO via X-ray photoelectron spectroscopy (XPS) measurements and first-principles density functional theory (DFT) calculations.[49] To the best of our knowledge, there are no reports describing the factors influencing the stability and packing density of short chain bifunctional linker molecules on polycrystalline ZnO surfaces, and their propensity for subsequent functionalization (such as catalyst immobilization). Inquires of this kind warrant an atomically precise visualization of the molecular adsorption process, a feature that cannot be accessed via conventional spectroscopic techniques. In this regard, the use of atom-probe tomography (APT) appears promising since it is able to provide chemical information with near atomic resolution in three dimensions.[50] APT can therefore be used to study the atomistic ordering and orientation of the SAMs and act as an effective supplement for other surface characterization techniques.

In this work, XPS, APT, and theoretical calculations were used to study the adsorption of 3-azidopropylthiol and 3-azidopropyltriethoxysilane SAMs (henceforth referred to as AzPT and AzPTES, respectively) on mono and polycrystalline ZnO surfaces. The influence of the surface polarity of ZnO (10$\bar{1}$0, 0001-O, and 0001-Zn) and the anchor group on the binding modes, stability, and packing density of the SAMs was determined (**Figure 1**). To demonstrate the applicability of linker-modified polycrystalline ZnO as a support for molecular heterogeneous catalysis, a chiral norbornadiene ligand with an alkyne side chain was clicked onto the azide terminal of the SAM via azide-alkyne cycloaddition,[51] and then complexed with a Rh precursor.[9,18] The thicknesses and packing densities of the SAMs were estimated via angle-resolved XPS (ARXPS) measurements. Temperature-dependent XPS (TDXPS) was used to analyze the thermal stability of the SAMs. APT measurements were performed to analyze the coverage and distribution of SAMs on the ZnO surface. Field evaporation thresholds were used to estimate the bonding strength of the linker molecules to the ZnO surface. DFT calculations and ab initio molecular dynamics (AIMD) calculations were employed to identify the effect of the anchor group and surface polarity on the interaction affinity and conformation of the linker molecules and their dynamical behavior on ZnO surfaces, respectively. The computational models were correlated with the results of the XPS and APT experiments to identify the optimum azide-terminated catalyst linker for polycrystalline ZnO surfaces.

2. Results and Discussion

2.1. Fabrication of Polycrystalline ZnO Films via Chemical-Bath Deposition

Polycrystalline ZnO films were deposited on Au coated Si substrates via chemical-bath deposition (CBD).[52] The sputtered Au layer acts as a template for the deposition of ZnO and ensures the formation of smooth and homogeneous ZnO films. For the CBD process, $Zn(OAc)_2 \cdot 2H_2O$ was used as the Zn precursor, polyvinylpyrrolidone (PVP) as the structure-directing agent and tetraethylammonium hydroxide (TEAOH) as an organic base catalyst. After ten deposition cycles, ZnO films with an average thickness of ≈100 nm could be obtained (**Figure 2**). The average surface roughness (R_a) of the obtained ZnO films as determined from atomic-force microscopy (AFM) measurements was 5.6 ± 0.7 nm (averaged over 5 different AFM images measuring 5 × 5 µm² each) (Figure S1, Supporting Information).

2.2. Experimental Studies of AzPT and AzPTES SAMs on Polycrystalline ZnO

AzPT and AzPTES SAMs were assembled on the fabricated polycrystalline ZnO films following reported procedures.[9,49,53] Experimental investigations into the binding modes, thickness, surface coverage and thermal stability of AzPT and AzPTES SAMs on polycrystalline ZnO surfaces are presented herein.

2.2.1. Polarization Modulation Infrared Reflection-Adsorption Spectroscopy (PM-IRRAS) Analysis

The immobilization of the SAMs on the ZnO surface was first confirmed via PM-IRRAS studies (**Figure 3**). The characteristic
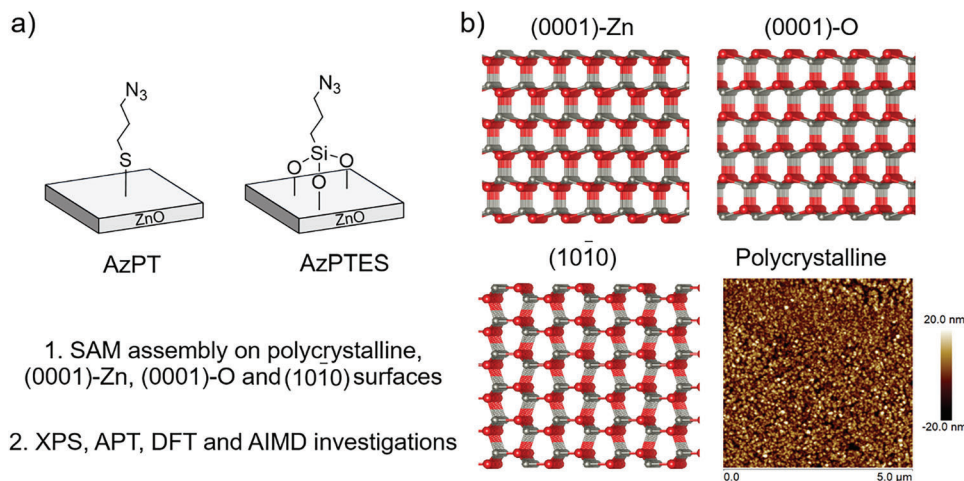
Figure 1. a) Molecular structures of AzPT and AzPTES SAMs on a ZnO surface and an overview of the experiments conducted in this study, b) ZnO surfaces investigated via XPS, represented as side-view ball and stick DFT atom maps for monocrystalline (0001)-Zn, (0001)-O, and (10$\bar{1}$0) ZnO (Grey: Zn; Red: O), and as an AFM image for polycrystalline ZnO.

asymmetric stretching mode of the azide group $\nu_a(N_3)$[54] is observed at ≈2100 cm^{-1} in both AzPT and AzPTES functionalized ZnO. The bands at 2860 and 2925 cm^{-1} in AzPT-ZnO and the bands at 2877 and 2931 cm^{-1} in AzPTES-ZnO are ascribed to the asymmetric $\nu_a(CH_2)$ and symmetric $\nu_s(CH_2)$ stretching modes of the methylene groups in the linkers, respectively.[25,55] The low-intensity peak at ≈1240 cm^{-1} in AzPTES-ZnO is assigned to the longitudinal optical mode of the asymmetric Si–O–Si stretch $\nu_a(Si–O)$, and indicates the presence of bridged siloxane groups.[48]

2.2.2. XPS Analysis of AzPT and AzPTES SAMs on Polycrystalline ZnO

XPS measurements were performed to study the local binding modes of the linker molecules (**Figures 4** and **5**). Peak assignments, binding energies (BEs) and other spectral details are provided in Table S2, Supporting Information. In the untreated polycrystalline ZnO film, the Zn $2p_{3/2}$ peak appears at 1021.5 eV, in good agreement with the expected peak position of Zn^{2+} sites in hexagonal wurtzite ZnO.[56] Attenuation of the Zn $2p_{3/2}$ peak is observed after AzPT and AzPTES functionalization due to inelastic scattering of the Zn 2p photoelectrons by the SAM.[47]

The asymmetric O 1s peaks in AzPT/AzPTES functionalized ZnO are fitted with two component peaks at BEs of ≈530.2 and 531.6 eV (Figures 4b,5b). These peaks are ascribed to the lattice oxygen anions of ZnO and non-lattice oxygen species (either surface hydroxyl groups of ZnO or oxygen atoms in the SAMs), respectively.[43]

The C 1s emission consists of three components (Figures 4c,5c). The most intense peak at 284.8 eV can be attributed to the C atoms present in the alkyl chain of the linkers as well as adventitious C. The peaks at 285.7 eV (for AzPT) and 286.0 eV (for AzPTES) correspond to C atoms in higher oxidation states or those attached to electron-withdrawing species, such as C–N or C–S.[57] The C 1s peak also exhibits pronounced tailing and a low intensity peak characteristic of oxidized carbon species (such as carbonyl groups) is observed at 289.1 eV (for AzPT) and 289.2 eV (for AzPTES).[32] The presence of such oxidized C species can be attributed to the adsorption of trace quantities of atmospheric CO$_2$ by the sample in the measurement chamber.[58] The N 1s emission consists of a single peak at ≈399.8 eV (for AzPT) and ≈400.1 eV (for AzPTES) (Figures 4d,5d). It is known that surface-bound azides decompose upon prolonged X-ray irradiation to form their corresponding imines.[59] Thus, the three distinct N species associated with the azide group coalesce
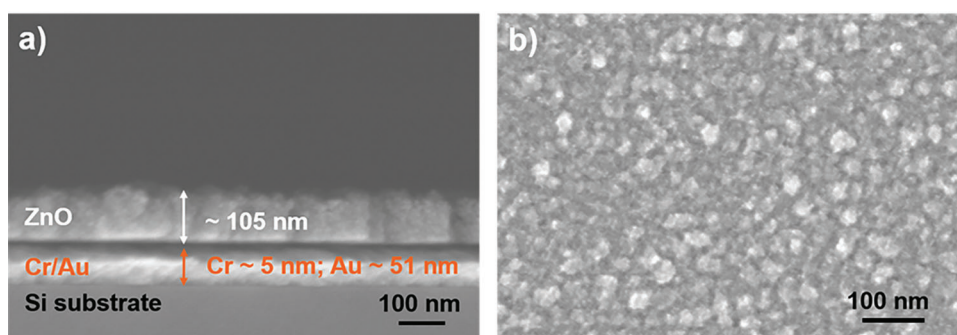

Figure 2. Scanning electron microscope (SEM) a) cross-section and b) top-view images of a polycrystalline ZnO film deposited on a Si/Cr/Au substrate via CBD.
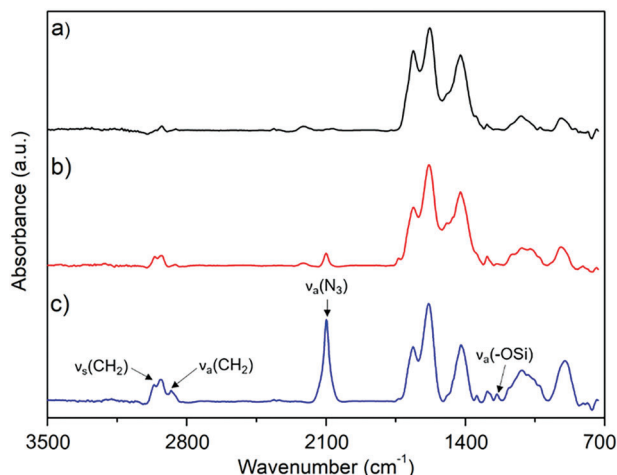
Figure 3. PM-IRRAS absorbance spectra of a) bare polycrystalline ZnO, b) AzPT, and c) AzPTES immobilized on polycrystalline ZnO (the structures of AzPT and AzPTES are shown as insets in (b) and (c)). The corresponding vibrational labels are included for reference.

to produce a single peak. The full-width at half-maxima (FWHM) of the measured N 1s peaks are relatively large (3.1–3.2 eV) and account for the presence of multiple chemically distinct nitrogen atoms of the azide group.

The S 2p peak in AzPT functionalized ZnO contains two principal components centered around ≈169.3 and 163.2 eV (Figure 4e). The respective peaks are further deconvoluted into doublets with a difference of ≈1.1 eV and an area ratio of 1:2, due to the spin-orbit splitting of S 2p into its S $2p_{3/2}$ and S $2p_{1/2}$ components.[60] The peak at 158.2 eV corresponds to a plasmon loss from the Zn 3s transition and is not related to sulfur.[21] The S $2p_{3/2}$ peak centered at 163.2 eV is indicative of thiolate S–Zn binding. The high energy S 2p peaks around 169.2 eV can be attributed to oxidized sulfur species (sulphonates).[46] The exact nature of this oxidized sulfur species is unclear, as it has been ascribed to both sulphonate (S–O–Zn) bond formation with the O atoms of the ZnO lattice[21] and the post factum oxidation of thiolate (S–Zn) SAMs.[19] Compositional analyses of the obtained XPS peaks indicate that the majority of sulfur in the AzPT functionalized ZnO samples exists in the oxidized form (**Table 1**). The Si 2p emission in AzPTES functionalized ZnO consists of a single intense peak at 101.9 eV (Figure 5e), consistent with siloxane species that can attach to the ZnO surface via the $(-O)_3$Si binding mode.[38] However, the large FWHM of this peak suggests a possible contribution from bridged siloxanes (Si–O–Si) as noted in the PM-IRRAS measurements.

In addition to peak positions, relative-sensitivity factor (RSF) corrected XPS peak areas were used to determine the local stoichiometry of the SAMs (Table 1). RSF correction allows XPS peak areas to be normalized relative to the composition of the corresponding element in the sample (detailed calculations of atomic ratios and equivalent homogeneous compositions are provided in the Supporting Information).[62] In the case of untreated polycrystalline ZnO, the ratio of normalized areas of the lattice O 1s peak (≈530 eV) to the Zn $2p_{3/2}$ peak ($O_{lattice}$/Zn) is ≈0.8, lower than the expected stoichiometric O/Zn ratio of 1 for an ideal ZnO lattice.[63–65] This is indicative of oxygen vacancies in the

underlying ZnO film, consistent with earlier reports on polycrystalline ZnO films produced via CBD.[66] The $O_{lattice}$/Zn ratios in the AzPT and AzPTES modified ZnO films are ≈0.7, within the expected error window (≈10%) for atomic ratios derived from normalized XPS peak areas.[67] More importantly, it is observed that SAM functionalization results in a discernible increase in the non-lattice (or overlayer) oxygen component at ≈531.6 eV, attributed to surface hydroxyls or oxygen atoms in the SAMs. In the case of AzPT functionalized polycrystalline ZnO, the ratio of the normalized areas of the sulphonate (≈169 eV) and thiolate (≈163 eV) S 2p peaks is 1.39, indicating that the dominant binding mode for AzPT is as sulphonate (S–O–Zn) rather than thiolate (S–Zn). This is comparable to the observations made by Ogata and coworkers for the adsorption of 1-propanethiol on polar (0001)-O ZnO.[31] On the other hand, the Si/O ratio in AzPTES functionalized polycrystalline ZnO is stoichiometric (≈0.3) and correlates well with the expected $(-O)_3$Si binding mode for AzPTES. However, it is unclear if all the −O−Si linkages are formed with the ZnO surface since some of the −O−Si groups can also interact with neighboring AzPTES molecules to form siloxane bridges.

It should also be noted that the atomic ratios described above are very rough approximations due to the low sampling depth of XPS (typically 50–100 Å).[68] Effective thicknesses and surface coverages of the SAMs can offer additional insights on the interaction between the anchor group of the linker and the stability of the SAMs. For polycrystalline ZnO, the measured thicknesses and surface coverages of AzPT and AzPTES are 4.84 ± 0.02, 4.81 ± 0.03 Å and 2.83 ± 0.02, 1.15 ± 0.03 molecules per nm², respectively (detailed calculations of the SAM thicknesses and surface coverages are provided in the Supporting Information). The SAM thicknesses are lower than the predicted lengths for the corresponding isolated molecules by around 2 Å (Figure S14, Supporting Information), indicating molecular tilting in the SAMs. The surface coverage of AzPT is intuitively greater than that of AzPTES due to its monodentate binding, which allows for more AzPT molecules to be packed together in a unit surface.

TDXPS measurements were then performed to assess the thermal stability of the SAMs. Although the intensities of the S 2p peaks decrease at higher temperatures, they do not completely disappear, implying the persistence of some physisorbed sulfur species on the ZnO surface, as noted in some earlier reports.[71] The C/S ratio diminishes upon annealing, and a large decrease is observed at 373 K (Table S5, Supporting Information), indicating the desorption of some adventitious C and a possible C−S scission at this temperature, similar to n-hexanethiol SAMs on ZnO.[21] In contrast, the Si/O ratios in AzPTES functionalized ZnO remain largely consistent even after annealing the samples at 473 K, thus demonstrating the increased thermal resistance of SAMs based on AzPTES.

2.3. APT Analysis of AzPT and AzPTES SAMs on ZnO

2.3.1. Determination of SAM Constitution and Surface Coverages via APT

APT measurements were performed to determine the relative binding strengths of AzPT and AzPTES and to verify some of
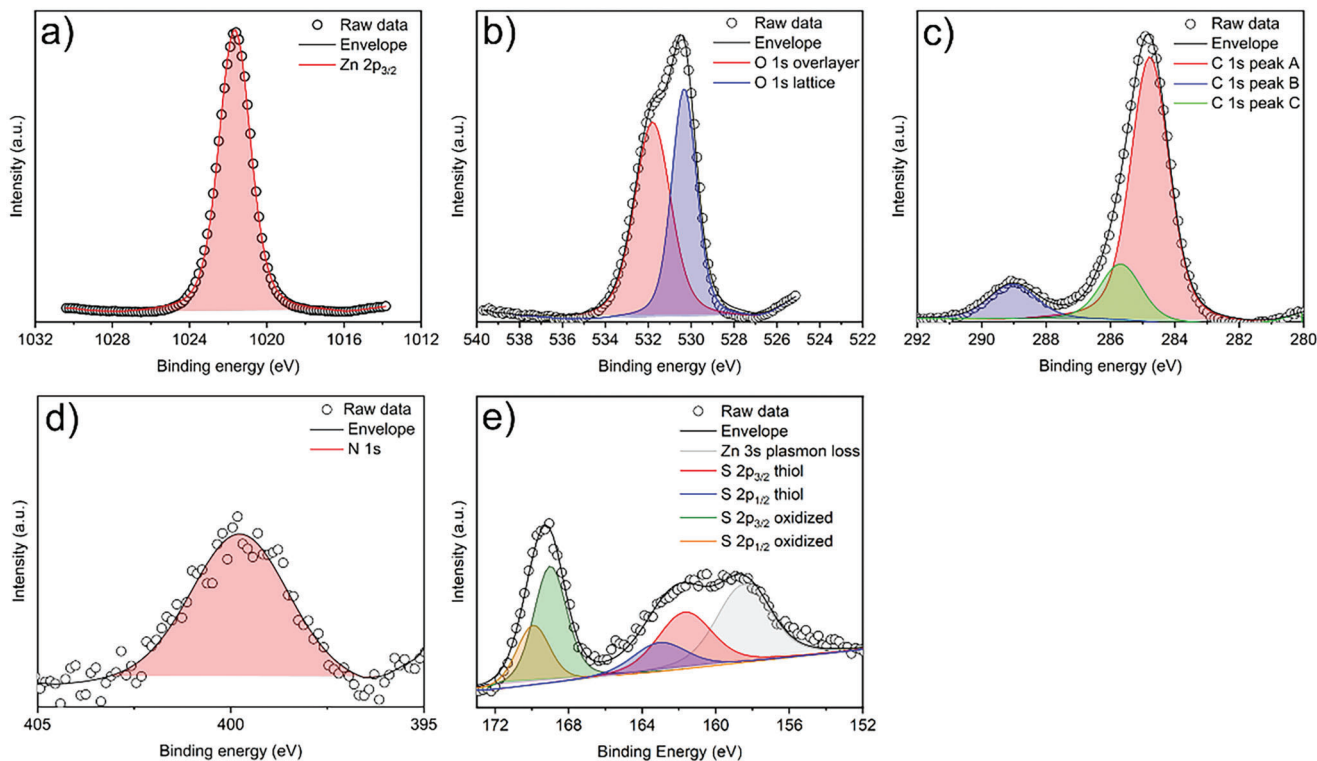
**ADVANCED
SCIENCE NEWS**

www.advancedsciencenews.com

**ADVANCED
MATERIALS
INTERFACES**
Open Access

www.advmatinterfaces.de

Figure 4. XPS spectra of AzPT immobilized on polycrystalline ZnO. The resolved a) Zn 2p$_{3/2}$, b) O 1s, c) C 1s, d) N 1s, and e) S 2p peaks are shown.
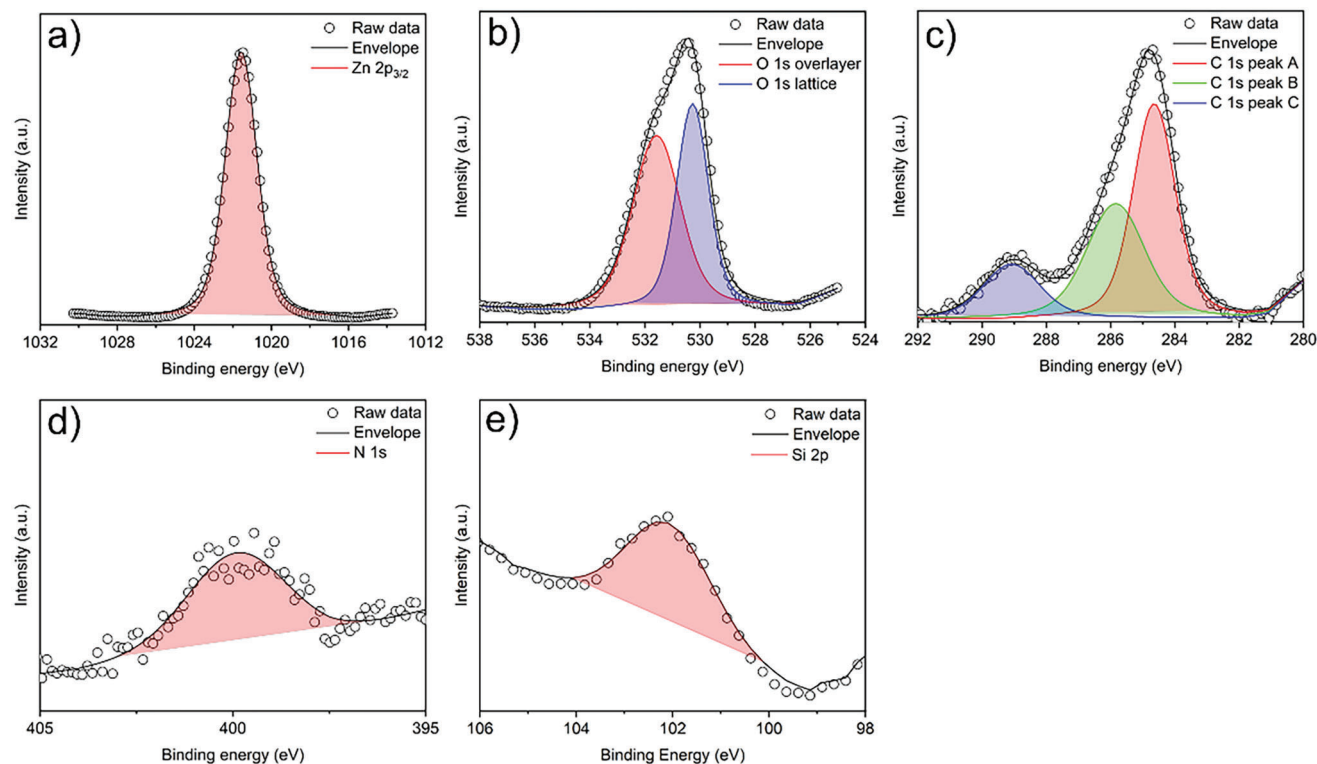

Figure 5. XPS spectra of AzPTES immobilized on polycrystalline ZnO. The resolved a) Zn 2p$_{3/2}$, b) O 1s, c) C1s, d) N 1s, and e) Si 2p peaks are shown.

2300399 (5 of 14)

Table 1. Ratios of normalized XPS peak areas of the elements analyzed in AzPT and AzPTES functionalized ZnO (calculated at 298 K).

ZnO surface	AzPT					AzPTES			
	$O_L/Zn^{a)}$	$O_O/O_L^{b)}$	S_{thiol}/Zn	S_{ox}/Zn	S_{ox}/S_{thiol}	O_L/Zn	O_O/O_L	Si/Zn	Si/O_O
Polycrystalline	0.70	1.25	0.07	0.10	1.39	0.65	1.26	0.24	0.29
(0001-O)	0.65	1.19	0.02	0.06	2.63	0.69	1.15	0.18	0.28
(0001-Zn)	0.49	1.01	0.04	0.03	0.73	0.44	1.13	0.14	0.29
($10\bar{1}0$)	0.88	0.50	0.25	0.04	0.17	0.78	0.72	0.15	0.27

a) O_L = O 1s Lattice; b) O_O = O 1s Overlayer.

the surface coverages obtained via ARXPS. For APT analysis, a single crystal ZnO substrate with ($10\bar{1}0$) orientation was chosen, since the polycrystalline ZnO substrates obtained via CBD failed prematurely due to high mechanical stresses induced by the electric field. The single crystalline substrate is a good approximation, since the tip dimensions are so small, that the measured volume in a polycrystalline film would effectively be constrained to a single crystal. The single crystal substrate shows very high stability during APT measurements and therefore results in reliable measurement conditions. Atom probe analysis of AzPT and AzPTES layers deposited on ZnO tips results in detection of positively charged molecular ions with low mass-to-charge (m/n) ratios. These signals occur in small groups of various peaks. In contrast, metallic specimens in APT usually evaporate as elemental ions with different charge states. The generated electric field is screened and penetrates only the very outmost atomic layer, the field inside the tip is zero. For non-conductive materials, the electric field can penetrate further into the material and therefore allows the evaporation of larger ion clusters. In the case of the adsorbed linkers, the individual molecules dissociate into small fragments and are detected as such in the time-of-flight mass spectra. **Figure 6**a depicts an exemplary mass spectrum of AzPTES on ZnO. Approximately 40 mass peaks are identified. The most abundant peak is $C_2H_5^+$ (29 u), which stems from the carbon backbone of the linker molecule. Nitrogen is detected in different forms, as NH^+ (15 u) in combination with residual hydrogen from the measurement chamber, as well as N_2^+ (28 u), N_3^+ (42 u), and various $N_2CH_y^+$ (40, 41 u) and $NC_3H_x^+$ (50–57 u) molecular ions. Please note that field evaporated species can

combine with hydrogen from the residual atmosphere within the measurement chamber. Si is detected in combination with O and H, that is, as SiO_2^{2+} (30 u), $SiOH^+$ and $SiOH_2^+$ (45, 46 u). No molecular ions consisting of Si and C are identified, therefore suggesting weaker C–Si bonds than Si–O bonds. The m/n positions of the peaks and their assigned species are given in Table S9, Supporting Information, for both monolayer systems. Figure 6b displays a representative mass spectrum of an AzPT measurement. The spectrum is normalized toward the highest mass signal, which is the $C_2H_5^+$ peak at 29 u, also in the case of AzPTES. Due to the linker molecules being almost identical, except for the headgroup, the mass spectra in Figure 6a,b appear similar. However, the intensity of the peaks displays a different distribution, therefore suggesting differentiation of the mass signals of the different linker molecules. Nitrogen is detected as N^+ (14 u), NH^+ (15 u), N_2^+ (28 u), $N_2CH_x^+$ (40, 41 u), and N_3^+ (42 u). The sulfur of the headgroup binding to the substrate is detected as molecular ions of SCH_x^+ (44–48 u) and $SC_2H_x^+$ (56–63 u).

Surface coverages of the linkers can also be obtained via APT. The number of the respective headgroup atoms is determined by integration of the mass peaks and splitting of the respective molecules. Si and S atoms are counted for AzPTES and AzPT, respectively. The surface area is then determined from the reconstructed volume, considering the surface area of the hemispherical endcap of the tip. Dividing the number of headgroup atoms by the surface area results in the coverage of the respective linker molecules. The average coverage of amounts to 0.6 ± 0.2 molecules per nm^2 for AzPTES and to 1.1 ± 0.4 molecules per nm^2 for AzPT. The thiol linker therefore shows a higher
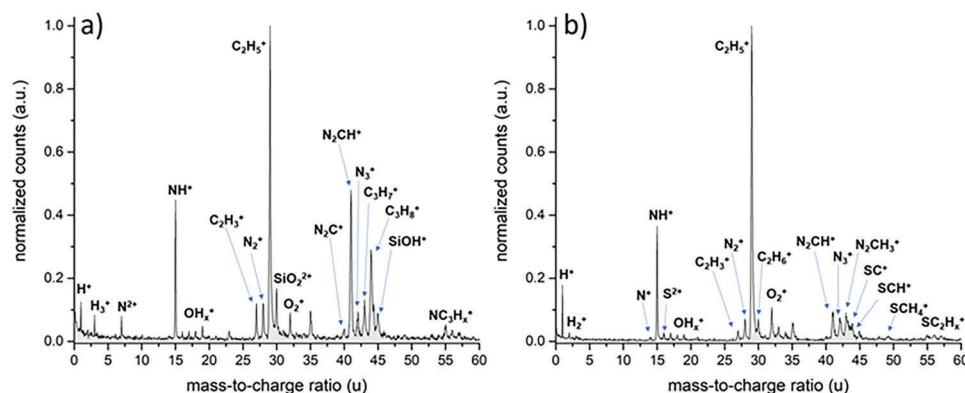

Figure 6. Typical mass spectra for a) AzPTES and b) AzPT measurement on ($10\bar{1}0$) ZnO showing different molecular ion signals. The mass spectra only contain the data of the AzPTES and AzPT layers.

2300399 (6 of 14)

**ADVANCED
SCIENCE NEWS**

www.advancedsciencenews.com

**ADVANCED
MATERIALS
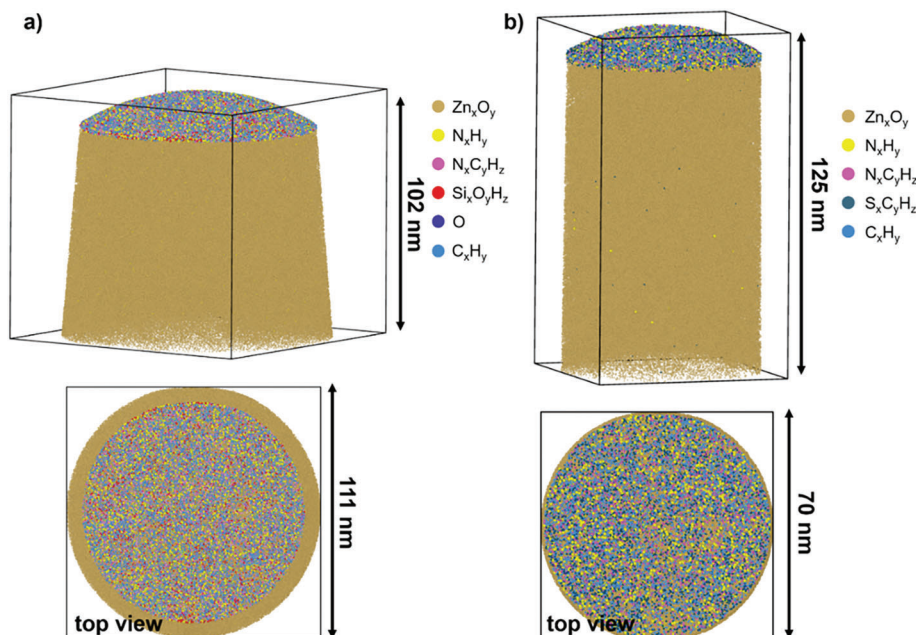INTERFACES**
Open Access

www.advmatinterfaces.de

Figure 7. Reconstructed 3D atom maps of a) AzPTES and b) AzPT on ZnO with their corresponding top-view images.

coverage on $(10\bar{1}0)$ ZnO than the corresponding silane linker. **Figure 7** shows the reconstructions of both measured linker systems on ZnO. A side view and a top view are shown respectively for both systems. Figure 7a shows an atom map of an AzPTES measurement, while Figure 7b displays an AzPT measurement. Molecules containing Zn and combinations of Zn and O are depicted in a golden color, while the remaining molecules stemming from the SAM are color-coded according to the legend given in Figure 7a,b. The monolayer is in both cases homogeneously distributed across the tips surface, which agrees well with our expectation for the non-polar homogeneous $(10\bar{1}0)$ surface. In contrast, in the case of polar and polycrystalline ZnO surfaces, domains reflecting the different terminations by O or Zn would be expected during atom probe tip analysis. It should also be noted that the field of view within the atom probe is limited to the opening angle of the counter electrode and the tip to detector distance. Therefore, only the central portion of the specimen is effectively detected, and the reconstructions make it appear like there is no SAM on the lateral surfaces.

2.3.2. Estimation of Relative Binding Strength from APT Data

The magnitude of the evaporation field strength is a characteristic value for different compounds and elements and can be associated with the binding energy since it is contained in the activation barrier for field evaporation.[72]

$$F_{\text{EV}} \sim \frac{4\pi\varepsilon_0}{n^3 e^3} Q_0^2 \tag{1}$$

$$Q_0 = \Lambda + \Sigma I_n + n\Phi \tag{2}$$

With F_{EV} being the evaporation field strength, ϵ_0 permittivity of the vacuum, n the charge state, e the elementary charge, Q_0 the

activation energy, Λ the binding energy, ΣI_n the sum of ionization energies, and Φ the work function of the emitter. The actual values are hard to access directly from the APT measurements. However, the evaporation field or threshold can be used as estimate for the relative binding strength of the different head groups to the ZnO substrate. The extremely thin monolayer does not influence the ZnO tip shape and therefore, does not alter the electric field conditions at the tip apex. All ZnO tips were pre-measured prior to coating, therefore end-voltage and end-radius of each tip are known. A mass spectrum of such a pre-measurement and a transmission electron microscope (TEM) micrograph of a ZnO tip are shown in Figure S12, Supporting Information. This is important since the evaporation field strength is determined from the applied voltage and the curvature radius of the tip. This is known for the ZnO substrate. Therefore, determining the voltage at which the organic species evaporate provides their respective evaporation field strengths. These fields are determined at the onset of the evaporation of the respective anchor group of the SAM, which amount to 15 ± 3 V nm^{-1} for AzPTES and 11 ± 1 V nm^{-1} for AzPT. Typical electric field curves for an AzPTES and AzPT measurement are shown in Figure S13, Supporting Information. The values are in good agreement with similar systems previously measured in the atom probe.[50] The silane monolayer has the higher evaporation field strength and therefore a stronger binding to the ZnO substrate can be concluded.

2.4. Atomistic Calculations of AzPT and AzPTES SAMs on ZnO

In addition to the length and anchor group of the linker molecules, the polarity of the ZnO surface is an important determinant of SAM stability, molecular orientation and surface coverage. As opposed to the non-polar $(10\bar{1}0)$ surface which
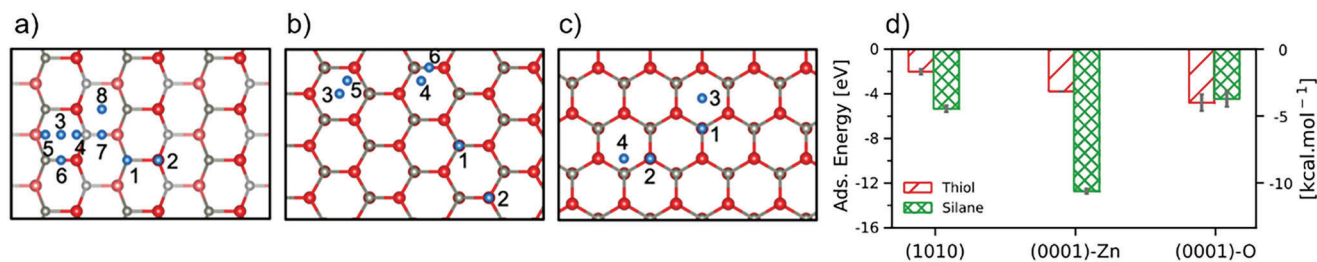
Figure 8. Top-view ball and stick models of a) (10$\bar{1}$0), b) (0001)-Zn, and c) (0001)-O ZnO surfaces. Zn atoms are shown in grey and O atoms in red. In the top view image of the (10$\bar{1}$0) surface (a), the atoms that are slightly lower than the surface atoms are shown in lighter colors for clarity. The possible adsorption sites on each surface are shown in blue and indexed to assist the discussion in the text, d) adsorption energy averaged over all potential adsorption sites, as calculated by DFT.

contains a symmetric distribution of O and Zn atoms, polar (0001) surfaces are nominally terminated with either O or Zn atoms (Figure 1b), and thus exhibit different reactivities toward SAM immobilization.[16] Hence, atomistic calculations were employed to understand the influence of ZnO surface polarity on the interaction affinity and conformational behavior of the AzPT and AzPTES. First, the potential adsorption sites on the various ZnO surfaces were identified using the CatKit package.[73] After performing a symmetry analysis to negate repeating adsorption sites, a total of 8, 6, and 4 potential adsorption sites were ascertained for the (10$\bar{1}$0), (0001)-Zn, and (0001)-O surfaces, respectively. The potential adsorption sites are shown in blue in **Figure 8**a–c, and are enumerated with indices. Adsorption site 1 is on top of a single Zn atom, while site 2 is on top of a single O atom. Site 3 is a hollow site. Site 4 is an O–O bridge, while site 5 is a Zn–Zn bridge. Site 6 is a Zn–O bridge. Site 7 is also a Zn–O

bridge, but the Zn and O atoms are located on two different atomic levels. Site 8 is also a hollow site similar to site 3, but the neighboring atoms are on different atomic levels in the crystal (Figure 8a).

Using DFT,[49] the adsorption energies of AzPT and AzPT on all the adsorption sites were calculated, and the preferred adsorption sites for AzPT and AzPTES on each ZnO surface were determined (**Table 2**). The average adsorption energies of AzPT and AzPTES on the different ZnO surfaces are also graphically shown in Figure 8c. For some adsorption sites, the optimization of the linker on the surface was not successful (for example, when the linker molecule moved away from the surface). Thus, no adsorption energy is reported in Table 2. The preferred adsorption sites after completion of energy optimization, for AzPT and AzPTES on the (10$\bar{1}$0), (0001)-Zn, and (0001)-O surfaces are similar to those indexed 5, 5, 4 and 5, 5, 1 in Figure 8, respectively. Herein,

Table 2. Relative adsorption energies of AzPT and AzPTES on the different adsorption sites of (10$\bar{1}$0), (0001)-Zn, and (0001)-O ZnO surfaces determined via DFT. The most favorable adsorption energies for each studied system are shown in bold text.

ZnO surface	Adsorption site index	AzPT		AzPTES	
		Adsorption energy [eV]	Average [eV]	Adsorption energy [eV]	Average [eV]
(10$\bar{1}$0)	1	−1.844	−2.012 ± 0.248	–	−5.343 ± 0.294
	2	−1.751		–	
	3	**−2.241**		**−5.498**	
	4	−2.240		−4.902	
	5	−2.239		−5.490	
	6	−1.846		−5.481	
	7	−2.240		–	
	8	−1.696		–	
(0001)-Zn	1	−3.771	−3.788 ± 0.018	−12.369	−12.691 ± 0.230
	2	−3.766		**−12.880**	
	3	−3.789		−12.487	
	4	−3.802		−12.845	
	5	**−3.812**		−12.872	
	6	−3.775		−12.869	
(0001)-O	1	**−5.206**	−4.779 ± 0.752	**−4.947**	−4.463 ± 0.684
	2	−3.656		–	
	3	−5.051		–	
	4	−5.201		−3.980	

it is important to note that when an adsorption site is reported as being the most favorable for a linker (such as site 5 for AzPT on on (10$\bar{1}$0)), the determination is made after initially placing the linker on a potential adsorption site, and then performing an energy optimization. The sites that produced the most favored adsorption after this optimization are considered to be the preferred adsorption sites. As can be seen in Table 2, the adsorption of AzPT on several initial adsorption sites of the (10$\bar{1}$0) surface (such as 3,4,5, and 7) have very close energies to that of the final energy of AzPT on site 5. Snapshots of AzPT and AzPTES molecules on the most favored adsorption sites before and after structural optimization via DFT are also shown in Figures S15 and S16, Supporting Information. On most of the analyzed surfaces, the linker molecules prefer to interact with the lattice Zn atoms either directly or via a bridging site. In so far as the non-polar (10$\bar{1}$0) surface is concerned, we had earlier reported that the symmetric distribution of surface Zn and O atoms is locally distorted upon AzPT adsorption to allow the thiol group to immobilize on the Zn−Zn bridging site 5.[49] A similar behavior is expected for AzPTES as well. The most energetically favorable ZnO surfaces for the adsorption of AzPT and AzPTES are polar (0001)-O and (0001)-Zn, respectively. The favorable adsorption of AzPT on the oxygen terminated (0001)-O surface indicates the increased tendency of AzPT to form S−O−Zn linkages with the ZnO lattice. The atomistic snapshots clearly show that the preferred adsorption mode for AzPT on (0001)-O is via bridging site 4, which allows for two concurrent S−O linkages (Figure S15, Supporting Information). On Zn-terminated surfaces such as (0001)-Zn and (10$\bar{1}$0), the adsorption of AzPT occurs primarily via S−Zn linkages between the thiol and the lattice Zn atoms. However, this kind of binding is associated with comparatively higher adsorption energies. In the case of AzPTES, it is posited from the calculations that the Zn terminated (0001)-Zn surface stabilizes the three oxygens in AzPTES more effectively than non-polar (10$\bar{1}$0), and oxygen terminated (0001)-O, thereby resulting in a more energetically favored adsorption. Understandably, the least favorable surface for the adsorption for AzPTES is (0001)-O, since it requires interactions between the O atoms of the linker and the surface O atoms of ZnO. With the exception of the (0001)-O surface, the adsorption of AzPTES is energetically more favorable than AzPT on all analyzed ZnO surfaces.

Having identified the ground state adsorption energies of the linkers, AIMD calculations of single AzPT and AzPTES molecules only on the most favorable adsorption sites for the different ZnO surfaces were carried out for a total simulation time of 20 ps (Figures S15 and S16, Supporting Information). The average molecular lengths of the linkers determined via AIMD calculations are reported in **Table 3**. When compared to ground state DFT calculations (Table S12, Supporting Information), a clear decrease in the molecular length is observed after dynamic sampling at room temperature. In almost all studied cases, the linker molecules appear to prefer a conformation that is tilted toward the surface. This can be attributed to charged interactions between the polar azide head group of the linkers and the surface Zn atoms. The extent of tilting is naturally higher on Zn-terminated surfaces such as (0001)-Zn or (10$\bar{1}$0) and can account for the low molecular lengths observed on these surfaces.

Table 3. Length of linker molecules (Å) along the z-axis on the ZnO surfaces determined via AIMD calculations.

ZnO surface[a]	AzPT	AzPTES
(10$\bar{1}$0)	(5) 2.55 ± 0.27	(5) 6.22 ± 0.62
(0001)-Zn	(5) 2.55 ± 0.13	(5) 3.56 ± 0.23
(0001)-O	(4) 3.53 ± 0.83	(1) 4.09 ± 0.19

[a] The AIMD values are averaged over a sampling time of 20 ps for only the most favorable adsorption site on each ZnO surface, as reported through the index in parentheses.

2.5. Experimental Investigations on the Influence of ZnO Surface Polarity on the Binding Modes of AzPT and AzPTES SAMs

Parallel to polycrystalline ZnO films, ZnO single crystals with non-polar (10$\bar{1}$0) and polar (0001)-O, (0001)-Zn surface terminations were also functionalized with AzPT and AzPTES and analyzed via ARXPS (**Figure 9**) to corroborate the findings of the DFT and AIMD calculations, and to better understand the influence of ZnO surface polarity on the binding modes of the linkers. Specifically, in the case of thiol SAMs, conflicting reports exist on the preferred binding mode (S−O−Zn vs S−Zn) for different ZnO surfaces.[19,21,31,46] The ARXPS results show that the binding mode of AzPT is strongly influenced by the surface polarity of ZnO (Figure 9a). While both sulphonate and thiolate species are observed on all analyzed surfaces, the extent of sulphonate binding is highest on polar (0001)-O ZnO, followed by polycrystalline, (0001)-Zn and non-polar (10$\bar{1}$0), as evidenced by the ratios of the normalized areas of the sulphonate and thiolate S 2p peaks (Table 1). Thiolate S−Zn appears to be the dominant binding mode on non-polar (10$\bar{1}$0) ZnO, in good agreement with APT measurements that show no discernible oxygen-bound sulphur species for AzPT on (10$\bar{1}$0) ZnO (Figure 6b). As reported earlier, the stabilization of thiolate linkages on non-polar (10$\bar{1}$0) ZnO is attributed to the energetically favored adsorption of AzPT on a bridging site between two neighboring Zn atoms of (10$\bar{1}$0) ZnO (site 5 in Figure 8a) via the formation of two S−Zn bonds.[49] The atomistic calculations described in Section 2.4 also suggest that the interaction of AzPT with lattice O atoms is favored on (0001)-O ZnO, further validating the large sulphonate content measured on the (0001)-O surface. Overall, the XPS, APT and simulation data indicate that the formation of sulphonate linkages in AzPT SAMs is mainly caused by the interaction of thiols with the O atoms in the ZnO sublattice and not by the post factum oxidation of thiolate S−Zn bonds. As a result, sulphonate linkages are favored on surfaces that accommodate surface oxygen atoms (such as (0001)-O ZnO), and thiolate linkages predominate on surfaces where Zn−S bonds can be stabilized (such as (10$\bar{1}$0)). In the case of AzPTES, no visible trend is observed in ARXPS measurements (Figure 9b), with the Si/O ratio remaining stoichiometric (≈0.3) on all ZnO surfaces (Table 1). This suggests that the nature of silane binding is largely consistent across all ZnO surfaces.

The SAM thicknesses and surface coverages estimated via ARXPS can offer additional insights on the molecular orientation of the SAMs on the different ZnO surfaces (**Table 4**). In general, submonolayer thicknesses are observed on all analyzed surfaces, indicating molecular tilting. It is also seen that the surface coverage of linkers is higher on polycrystalline ZnO than
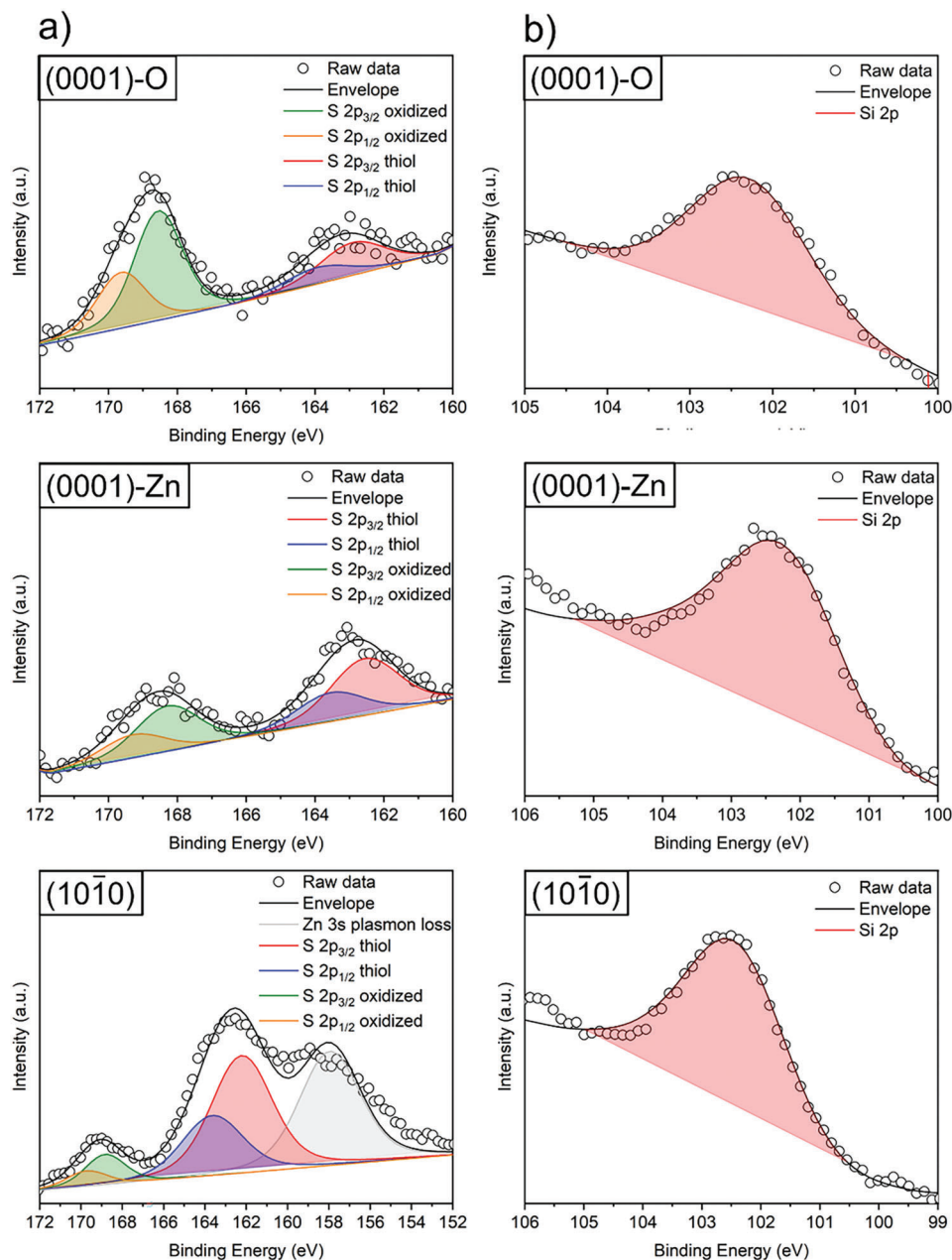
Figure 9. XPS a) S2p and b) Si 2p spectra for AzPT and AzPTES SAMs immobilized on (0001)-O, (0001)-Zn and (10$\bar{1}$0) ZnO surfaces.

all other monocrystalline surfaces. This is intuitive since a polycrystalline ZnO film consists of multiple random ZnO facets on which the SAMs can be immobilized. In addition to the obvious differences in surface polarity, factors such as crystal defects and grain boundaries can strongly influence SAM stability and surface coverage.[35,37,74,75] On polycrystalline ZnO, SAM stability and tilt are stochastically chosen among all different possibilities. Thus, the SAM thicknesses determined via ARXPS include contributions from all the ZnO surfaces present in the sample. Among the single crystal ZnO surfaces, SAM thicknesses and surface coverages are highest on polar (0001)-O, followed by nonpolar (10$\bar{1}$0) and polar (0001)-Zn. It is posited that the extent of

molecular tilting is greater on Zn terminated surfaces such as (0001)-Zn and (10$\bar{1}$0) due to the interaction between the negatively charged azide head group of the SAMs and the surface Zn atoms. On the (0001)-O surface that is nominally terminated with oxygen atoms, this interaction is repulsive in nature, and therefore, results in a lower tilt. It is also surmised that the higher SAM tilt on Zn-terminated surfaces offsets the surface coverage of SAMs, leading to fewer molecules being immobilized per unit area. The SAM thicknesses measured via ARXPS (Table 4) can be well correlated with the dynamic behavior of SAMs predicted by AIMD calculations (Table 3). In the case of AzPTES, some discrepancies are observed between the SAM thicknesses mea-

Table 4. Average thicknesses and surface coverages of AzPT and AzPTES SAMs on the studied ZnO surfaces estimated via ARXPS measurements.

ZnO surface[a]	SAM thickness [Å]		Surface coverage [molecules per nm²]	
	AzPT	AzPTES	AzPT	AzPTES
Polycrystalline	4.84 ± 0.02	4.81 ± 0.03	2.83 ± 0.02	1.15 ± 0.03
(10$\bar{1}$0)	2.94 ± 0.03	2.50 ± 0.05	1.72 ± 0.03	0.60 ± 0.05
(0001)-O	3.11 ± 0.08	3.25 ± 0.07	1.82 ± 0.08	0.78 ± 0.07
(0001)-Zn	2.31 ± 0.10	2.54 ± 0.08	1.35 ± 0.10	0.92 ± 0.08

[a] All calculations were performed by considering the attenuation of the Zn $2p_{3/2}$ photoelectron line using an inelastic mean free path (IMFP) value of 11.54 Å. The intrinsic uncertainty in the IMFP used for the evaluation of SAM thicknesses is estimated to be around 20.5%.[76] A detailed description of the variation of SAM film thicknesses with the IMFP values is provided in the Supporting Information.

sured by ARXPS/APT and those predicted by AIMD. This can be attributed to the influence of polysiloxane formation on tilting, which is not considered during AIMD sampling.

2.6. Immobilization of a Chiral Diene Ligand and Rh Complex on AzPTES Functionalized Polycrystalline ZnO

The stronger binding strength and thermal stability of AzPTES compared to AzPT makes it a more suitable linker for the attachment of molecular catalysts to the ZnO surface. As a proof of principle, a chiral norbornadiene ligand was tethered to AzPTES functionalized polycrystalline ZnO via azide-alkyne cycloaddition and then complexed with a Rh precursor to obtain an immobilized molecular catalyst capable of catalyzing asymmetric 1,2-addition reactions (**Scheme 1**).[9,18] While this immobilization pathway has been previously used to attach Rh-based chiral catalysts to SiO₂ surfaces,[9,18] its applicability for metal oxide surfaces, such as ZnO is unexplored.

The attachment of the chiral ligand and the corresponding Rh complex on AzPTES functionalized ZnO was therefore studied via XPS (**Figure 10**). For the clicked ligand on AzPTES functionalized ZnO, two N 1s peaks at BEs of 399.9 and 401.6 eV are observed (Figure 10a). These peaks can be attributed to the triazole and amide nitrogens, respectively. Similarly, a large increase in the atomic ratio of C confirms the inclusion of an additional organic component (from the norbornadiene and phenyl

groups of the ligand) to AzPTES. Trace amounts of the Cu catalyst used for the azide-alkyne cycloaddition could also be noted in the XPS analysis, consistent with observations made in earlier reports.[77] For the chiral Rh-diene complex, the characteristic $3d_{5/2}$ and $3d_{3/2}$ spin-orbit components of Rh appear at 309.8 and 314.8 eV, significantly higher than the expected peak positions for metallic Rh(0) species (Figure 10b).[78] This confirms the existence of Rh(I) in the immobilized catalyst, which correlates well with previous works in which the oxidation states of similar Rh-based molecular catalysts were studied using X-ray absorption spectroscopy.[79] The thicknesses of the chiral diene ligand and the Rh catalyst on AzPTES functionalized ZnO were determined using ARXPS measurements to be 4.5 ± 0.02 and 4.3 ± 0.02 Å, respectively. The corresponding surface coverages are 0.97 ± 0.02 and 0.31 ± 0.02 molecules per nm². The observed thicknesses are much smaller than the predicted molecular lengths for the SAM and ligand. This indicates a very high degree of molecular tilting or even a case of surface collapse due to the interaction between the charged Rh complex and the ZnO surface.[80] However, investigations beyond the scope of the current work are required to clarify this observation.

3. Conclusions

A combined experimental and theoretical approach was used to study the molecular adsorption of 3-azidopropylthiol (AzPT) and 3-azidopropyltriethoxysilane (AzPTES) catalyst linkers on poly and monocrystalline ZnO surfaces. It was observed that the binding mode of AzPT was strongly dependent on the ZnO surface polarity, varying from sulphonate-dominant for polar and polycrystalline ZnO to thiolate-dominant for non-polar ZnO. On the other hand, the (−O₃)Si binding mode of AzPTES remained consistent across all analyzed surfaces. TDXPS measurements also revealed a higher thermal stability for the silane over the thiol, with the latter undergoing probable dissociation between 373–473 K. The attenuation of the ZnO substrate XPS signal was used to estimate the thickness and surface coverage of the linkers via ARXPS. The thicknesses of AzPT and AzPTES SAMs on polycrystalline ZnO were in the order of ≈4.8 Å, while their surface coverages were around 2.1 and 1.1 molecules per nm², respectively. A similar evaluation of monocrystalline (0001)-O, (0001)-Zn, and (10$\bar{1}$0) surfaces showed lower surface coverages for both SAMs when compared to polycrystalline ZnO. Among the monocrystalline surfaces, the highest coverages of AzPT and
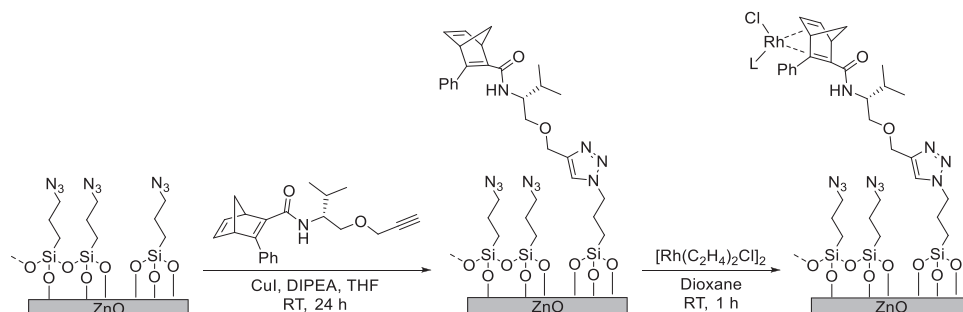
Scheme 1. Immobilization of a chiral diene ligand on AzPTES functionalized polycrystalline ZnO and its subsequent complexation with an Rh precursor to produce an asymmetric molecular heterogeneous catalyst tethered to ZnO. For clarity, the modification of only one linker molecule is shown in each panel.
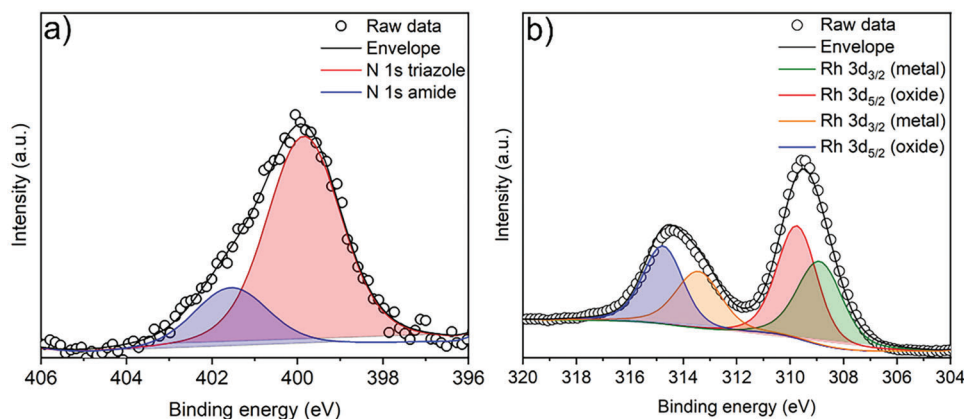
Figure 10. XPS spectra of the chiral Rh norbornadiene complex attached to AzPTES-functionalized polycrystalline ZnO. The resolved a) N 1s and b) Rh 3d peaks are shown.

AzPT were observed on the polar (0001)-O and (0001)-Zn surfaces, respectively. This behavior was attributed to charged interactions between the polar head group the linkers and the surface Zn atoms of ZnO. In all cases of monocrystalline ZnO, the thicknesses of the SAMs were lower than the isolated molecular lengths predicted via DFT calculations, indicating a high degree of tilting. Surface coverages of AzPT and AzPTES SAMs on ($10\bar{1}0$) ZnO calculated via 3D APT reconstructions corroborated the XPS measurements. The relative binding strengths for AzPT and AzPTES SAMs were determined via APT to be 11 ± 1 and 15 ± 3 V nm^{-1}, respectively, confirming the higher interaction affinity between the silane and ZnO predicted by molecular calculations. Overall, the experimental and theoretical results show that the adsorption of silane SAMs on ZnO is associated with a higher interaction affinity, binding strength, and thermal stability than the corresponding thiol. To demonstrate the applicability of AzPTES modified polycrystalline ZnO as a solid-state support for molecular heterogeneous catalysis, a chiral norbornadiene ligand was successfully appended to it via click chemistry and complexed with an Rh precursor. The thickness and surface coverage of the immobilized Rh complex were lower than those of the pure linker, due to possible surface collapse. While the immediate ramifications of this behavior are unclear, efforts are currently underway to study the catalytic performance of molecular catalysts immobilized on ZnO functionalized with azide-terminated silane linkers.

4. Experimental Section

Preparation of Substrates for AzPT and AzPTES Immobilization: The polished Si substrates used the deposition of polycrystalline ZnO films were cleaned prior to use via the following protocol: 1) sonication for 10 min in Milli-Q H$_2$O (resistivity 18.2 Ω cm), 2) sonication for 10 min in a 1:1 v/v solution of acetone and EtOH, 3) O$_2$-plasma treatment for 10 min (30 W under an O$_2$ flow rate of 55 cm^3 s^{-1}), and 4) sonication for 10 min in Milli-Q H$_2$O. The substrates were washed ten times with the corresponding solvent after each sonication step and dried under an N$_2$ stream. The substrates were then sputtered with 5 nm of Cr and 50 nm of Au via ion-beam sputtering under UHV conditions. The single crystal ZnO substrates (($10\bar{1}0$) and 0001) were washed with EtOH and dried under an N$_2$ stream before use.

Fabrication of Polycrystalline ZnO Films via CBD: The deposition of ZnO the Si/Cr/Au substrates was performed in accordance with a reported procedure.[52] Briefly, stock methanolic solutions of Zn(OAc)$_2$·2H$_2$O (34 mm), PVP (21.7 mm), and TEAOH (75 mm) were first prepared. The deposition solution was prepared by mixing the Zn(OAc)$_2$·6H$_2$O and PVP stock solutions in a ratio of 1:1 v/v. One volume unit of TEAOH was then added dropwise to the above solution at a rate of 1.04 mL min^{-1} via a peristaltic pump under continuous stirring. For mineralization, the substrates were placed in a sealed glass vessel with 1 mL of the deposition solution and then transferred to an oil bath at 60 °C for 1.5 h (for 1 deposition cycle). For additional deposition cycles, the substrates were removed from the deposition solution, washed thoroughly with MeOH, dried under an N$_2$ stream and reintroduced into a fresh 1 mL aliquot of the deposition solution. Ten such deposition cycles were carried out. After ZnO deposition, the films were thoroughly dried under an N$_2$ stream and then subjected to O$_2$ plasma treatment (30 W for 10 min at an O$_2$ flow rate of 55 cm^3 s^{-1}) to render the surface hydrophilic and to remove residual organic contaminants before immobilizing the linker molecules.

Immobilization of AzPT and AzPTES on ZnO: The immobilization of AzPTES and AzPT on the different ZnO surfaces was performed in accordance with the authors' earlier experimental reports.[9,49] For both AzPTES and AzPT, the polycrystalline ZnO films and monocrystalline ZnO substrates were placed in the corresponding linker solution and the SAMs were allowed to assemble on the ZnO surface for 24 h. After assembly, the unreacted SAMs were washed away with the corresponding solvent (EtOH for thiol, and toluene for silane). The substrates were then withdrawn, dried under an N$_2$ stream, and used for XPS analysis.

Immobilization of Chiral Norbornadiene Ligand and Rh Complex on AzPTES Functionalized Polycrystalline ZnO: The chiral norbornadiene ligand was synthesized according to a reported procedure from our earlier publication.[18] The alkyne-functionalized ligand was immobilized on the AzPTES functionalized polycrystalline ZnO films through a copper-catalyzed azide-alkyne cycloaddition (Scheme 1). Therefore, in a flame dried Schlenk tube under N$_2$ atmosphere, 5.00 mg (14.9 µmol) of the ligand were dissolved in 4 mL abs. THF, and then 1.83 µL (10.5 µmol) DIPEA and 2.00 mg (10.5 µmol) of CuI were added. The reaction mixture was stirred for 10 min at room temperature, the stirring bar was removed and two substrates with the AzPTES functionalized polycrystalline ZnO film were vertically placed in the solution and allowed to react for 24 h at room temperature. The substrates were retrieved and washed with 1 mL of acetone, 1 mL of water, and 1 mL of acetone, respectively. One of the substrates was then placed in a solution of 2.00 mg (5.14 µmol) [Rh(C$_2$H$_4$)$_2$Cl]$_2$ in 4 mL dioxane for 1 h at room temperature for the formation of the catalytic Rh diene complex. The substrate was removed and washed with 1 mL of dioxane, 1 mL of water and 1 mL acetone, respectively.

Characterization Methods: The Si substrates used for the deposition of polycrystalline ZnO films were first sputtered with 5 nm of Cr followed by 50 nm of Au via ion-beam sputtering under ultra-high vacuum (UHV) conditions (Veeco DC ion gun, base pressure $< 10^{-7}$ mbar). Scanning-electron microscope images were recorded on a Zeiss Merlin SEM operating at 3 kV. Prior to analysis, the samples were sputtered with 5 nm of Ir to render the surface conductive. Atomic force microscope (AFM) images were recorded on Bruker Digital Instruments MultiMode 8 AFM operating in tapping mode. Si cantilevers and PPP-NCHR-W $n+$ dope tips (Nanosensors, Switzerland) with a resistivity of 0.01–0.02 Ω cm were used. X-ray diffraction (XRD) measurements were done on a Rigaku Smartlab XRD setup using Cu-Kα radiation with a Hypix 3000 detector. Nuclear magnetic resonance (NMR) spectra were obtained from a Bruker Avance 300 (^{1}H, 300 MHz; ^{13}C, 75 MHz) spectrometer at room temperature. The NMR spectra were referenced to tetramethylsilane ($\delta = 0.00$ ppm) and calibrated on the residual solvent peak of $CDCl_3$. Spectral processing was done using a CD/Spectrus processing software. Polarization-modulation infrared reflection absorption spectroscopy (PM-IRRAS) measurements were performed on a Bruker PMA50 IRRAS setup equipped with a Hinds Instruments PEM-100 controller. All measurements were done at room temperature and ambient pressure with polarizer and detector angles of 0° and 80°, respectively. Angle-resolved XPS (ARXPS) measurements were performed using a Thermo Scientific Theta Probe ARXPS system. A parallel angle detector was used to measure the photoelectron signals emitted at an angular range of ≈20–80° from the sample surface without physically tilting the sample. For stimulating the photoemission, a non-monochromatic twin-gun X-ray source (Al-Kα, 1486.6 eV photon energy, 100 W operating power) was used. The XPS spectra were recorded at a pass energy of 200 eV (survey scan, 1 eV step, 50 ms dwell time) with several pass energy steps (single peaks, snap scan mode with 400–700 frames, 1 s scan time for each frame). To account for sample charging, the binding energies of all the peaks were calibrated with respect to the adventitious C 1s reference peak set up at 284.8 eV. Background correction was performed with a smart background function. The peaks were then fit with Voigt functions that were ≈30% Lorentzian and ≈70% Gaussian using the software ThermoAvantage V5.9919. For quantitative analysis, the following relative sensitivity factor (RSF) values provided by the ThermoAvantage software library were used (C 1s: 1, Zn 2p$_{3/2}$: 18.92; N 1s: 1.8; O 1s: 2.93; S 2p$_{3/2}$: 1.11; Si 2p: 0.817). For the determination of SAM thicknesses, an IMFP of 11.54 Å, corresponding to the peak BE of the Zn 2p$_{3/2}$ was used. Detailed procedures for the determination of the equivalent homogeneous compositions of the elements and the SAM thicknesses and surface coverages are provided in the Supporting Information.

Supporting Information

Supporting Information is available from the Wiley Online Library or from the author.

Acknowledgements

Conflict of Interest

The authors declare no conflict of interest.

Data Availability Statement

The data that support the findings of this study are available from the corresponding author upon reasonable request.

Keywords

[1] A. Küchler, M. Yoshimoto, S. Luginbühl, F. Mavelli, P. Walde, *Nat. Nanotechnol.* **2016**, *11*, 409.

[2] B. Mitschke, M. Turberg, B. List, *Chem* **2020**, *6*, 2515.

[3] S. H. A. M. Leenders, R. Gramage-Doria, B. de Bruin, J. N. H. Reek, *Chem. Soc. Rev.* **2015**, *44*, 433.

[4] F. Ziegler, J. Teske, I. Elser, M. Dyballa, W. Frey, H. Kraus, N. Hansen, J. Rybka, U. Tallarek, M. R. Buchmeiser, *J. Am. Chem. Soc.* **2019**, *141*, 19014.

[5] S. T. Emmerling, F. Ziegler, F. R. Fischer, R. Schoch, M. Bauer, B. Plietker, M. R. Buchmeiser, B. V. Lotsch, *Chemistry* **2022**, *28*, e202104108.

[6] A. Dhakshinamoorthy, A. M. Asiri, H. Garcia, *ChemCatChem* **2020**, *12*, 4732.

[7] I. Sinha, P. S. Mukherjee, *Inorg. Chem.* **2018**, *57*, 4205.

[8] S. R. Kousik, F. Ziegler, D. Sipp, A. Rodríguez-Camargo, H. Solodenko, W. Gassner, G. Schmitz, B. V. Lotsch, M. R. Buchmeiser, K. Koynov, P. Atanasova, *ACS Appl. Nano Mater.* **2022**, *5*, 14733.

[9] M. Deimling, S. R. Kousik, K. Abitaev, W. Frey, T. Sottmann, K. Koynov, S. Laschat, P. Atanasova, *ChemCatChem* **2021**, *13*, 2242.

[10] F. Ziegler, H. Kraus, M. J. Benedikter, D. Wang, J. R. Bruckner, M. Nowakowski, K. Weißer, H. Solodenko, G. Schmitz, M. Bauer, N. Hansen, M. R. Buchmeiser, *ACS Catal.* **2021**, *11*, 11570.

[11] P. Verma, Y. Kuwahara, K. Mori, R. Raja, H. Yamashita, *Nanoscale* **2020**, *12*, 11333.

[12] A. Kołodziejczak-Radzimska, T. Jesionowski, *Materials* **2014**, *7*, 2833.

[13] Ü. Özgür, Y. I. Alivov, C. Liu, A. Teke, M. A. Reshchikov, S. Doğan, V. Avrutin, S.-J. Cho, H. Morkoç, *J. Appl. Phys.* **2005**, *98*, 041301.

[14] M. A. Borysiewicz, *Crystals* **2019**, *9*, 505.

[15] M. Laurenti, S. Stassi, G. Canavese, V. Cauda, *Adv. Mater. Interfaces* **2017**, *4*, 1600758.

[16] R. M. Hewlett, M. A. McLachlan, *Adv. Mater.* **2016**, *28*, 3893.

[17] S. P. Pujari, L. Scheres, A. T. M. Marcelis, H. Zuilhof, *Angew. Chem., Int. Ed.* **2014**, *53*, 6322.

[18] A.-K. Beurer, M. Kirchhof, J. R. Bruckner, W. Frey, A. Baro, M. Dyballa, F. Giesselmann, S. Laschat, Y. Traa, *ChemCatChem* **2021**, *13*, 2407.

[19] P. W. Sadik, S. J. Pearton, D. P. Norton, E. Lambers, F. Ren, *J. Appl. Phys.* **2007**, *101*, 104514.

[20] K. Ozawa, M. Suzuki, R. Tochikubo, H. Kato, Y. Sugizaki, K. Edamoto, K. Mase, *J. Phys. Chem. C* **2016**, *120*, 8653.

[21] C. L. Perkins, *Phys. Chem. C* **2009**, *113*, 18276.

[22] C. Wöll, *Prog. Surf. Sci.* **2007**, *82*, 55.

[23] C. Vericat, M. E. Vela, G. Benitez, P. Carro, R. C. Salvarezza, *Chem. Soc. Rev.* **2010**, *39*, 1805.

[24] A. Ulman, J. E. Eilers, N. Tillman, *Langmuir* **1989**, *5*, 1147.

[25] T. Elzein, A. Fahs, M. Brogly, A. Elhiri, B. Lepoittevin, P. Roger, V. Planchot, *J. Adhes.* **2013**, *89*, 416.

[26] J. Singh, J. Im, E. J. Watters, J. E. Whitten, J. W. Soares, D. M. Steeves, *Surf. Sci.* **2013**, *609*, 183.

[27] S.-Z. Deng, H.-M. Fan, M. Wang, M.-R. Zheng, J.-B. Yi, R.-Q. Wu, H.-R. Tan, C.-H. Sow, J. Ding, Y.-P. Feng, K.-P. Loh, *ACS Nano* **2010**, *4*, 495.

[28] O. C. Grimm, R. M. D. S. Somaratne, Y. Wang, S. Kim, J. E. Whitten, *Phys. Chem. Chem. Phys.* **2021**, *23*, 8309.

[29] S. Bai, Y. Jin, X. Liang, Z. Ye, Z. Wu, B. Sun, Z. Ma, Z. Tang, J. Wang, U. Würfel, F. Gao, F. Zhang, *Adv. Energy Mater.* **2015**, *5*, 1401606.

[30] J. Singh, J. Im, J. E. Whitten, J. W. Soares, D. M. Steeves, *Langmuir* **2009**, *25*, 9947.

[31] K. Ogata, T. Hama, K. Hama, K. Koike, S. Sasa, M. Inoue, M. Yano, *Appl. Surf. Sci.* **2005**, *241*, 146.

[32] J. W. Soares, J. E. Whitten, D. W. Oblas, D. M. Steeves, *Langmuir* **2008**, *24*, 371.

[33] B.-A. Fouetio Kengne, S. Karmakar, M. Kaura, V. V. R. Sai, G. Corti, I. B. Niraula, A. Larin, J. Hall, D. Sowell, P. J. Hrdlicka, V. Dobrokhotov, D. N. McIlroy, *ACS Appl. Mater. Interfaces* **2014**, *6*, 13355.

[34] Y. Tong, T. Jiang, S. Qiu, K. Koshmak, A. Giglia, S. Kubsky, A. Bendounan, L. Chen, L. Pasquali, V. A. Esaulov, H. Hamoudi, *J. Phys. Chem. C* **2018**, *122*, 2880.

[35] A. Kornherr, G. E. Nauer, A. A. Sokol, S. A. French, C. R. A. Catlow, G. Zifferer, *Langmuir* **2006**, *22*, 8036.

[36] R. M. Petoral, G. R. Yazdi, A. L. Spetz, R. Yakimova, K. Uvdal, *Appl. Phys. Lett.* **2007**, *90*, 223904.

[37] A. Kornherr, S. Hansal, W. E. G. Hansal, J. O. Besenhard, H. Kronberger, G. E. Nauer, G. Zifferer, *J. Chem. Phys.* **2003**, *119*, 9719.

[38] C. G. Allen, D. J. Baker, J. M. Albin, H. E. Oertli, D. T. Gillaspie, D. C. Olson, T. E. Furtak, R. T. Collins, *Langmuir* **2008**, *24*, 13393.

[39] C. L. Xu, L. Fang, F. Wu, Q. L. Huang, B. Yin, *Colloids Surf., A* **2014**, *444*, 48.

[40] T. M. Brenner, G. Chen, E. P. Meinig, D. J. Baker, D. C. Olson, R. T. Collins, T. E. Furtak, *J. Mater. Chem. C* **2013**, *1*, 5935.

[41] R. R. Rye, G. C. Nelson, M. T. Dugger, *Langmuir* **1997**, *13*, 2965.

[42] O. Taratula, E. Galoppini, D. Wang, D. Chu, Z. Zhang, H. Chen, G. Saraf, Y. Lu, *J. Phys. Chem. B* **2006**, *110*, 6506.

[43] P. J. Hotchkiss, M. Malicki, A. J. Giordano, N. R. Armstrong, S. R. Marder, *J. Mater. Chem.* **2011**, *21*, 3107.

[44] W. Feng, A. S. Wan, E. Garfunkel, *J. Phys. Chem. C* **2013**, *117*, 9852.

[45] S. Hövel, C. Kolczewski, M. Wühn, J. Albers, K. Weiss, V. Staemmler, C. Wöll, *J. Chem. Phys.* **2000**, *112*, 3909.

[46] N. S. Pesika, Z. Hu, K. J. Stebe, P. C. Searson, *J. Phys. Chem. B* **2002**, *106*, 6985.

[47] J. Chen, R. E. Ruther, Y. Tan, L. M. Bishop, R. J. Hamers, *Langmuir* **2012**, *28*, 10437.

[48] B. Torun, I. Giner, G. Grundmeier, O. Ozcan, *Surf. Interface Anal.* **2017**, *49*, 71.

[49] P. Atanasova, M. Dou, S. R. Kousik, J. Bill, M. Fyta, *RSC Adv.* **2021**, *11*, 5466.

[50] H. Solodenko, P. Stender, G. Schmitz, *Microsc. Microanal.* **2022**, *28*, 1300.

[51] M. Meldal, C. W. Tornøe, *Chem. Rev.* **2008**, *108*, 2952.

[52] S. R. Kousik, D. Sipp, K. Abitaev, Y. Li, T. Sottmann, P. Koynov, P. Atanasova, *Nanomaterials* **2021**, *11*, 196.

[53] S. Kantheti, R. Narayan, K. V. Raju, *Polym. Int.* **2015**, *64*, 267.

[54] V. Jangid, D. Brunel, E. Sanchez-Adaime, A. K. Bharwal, F. Dumur, D. Duché, M. Abel, M. Koudia, T. Buffeteau, C. A. Nijhuis, G. Berginc, C. Lebouin, L. Escoubas, *Langmuir* **2022**, *38*, 3585.

[55] L. Rouvière, N. Al-Hajj, J. Hunel, C. Aupetit, T. Buffeteau, L. Vellutini, E. Genin, *Langmuir* **2022**, *38*, 6464.

[56] N. Pauly, F. Yubero, J. P. Espinós, S. Tougaard, *Surf. Interface Anal.* **2019**, *51*, 353.

[57] M. A. Caipa Campos, J. M. J. Paulusse, H. Zuilhof, *Chem. Commun.* **2010**, *46*, 5512.

[58] J. Singh, J. Im, J. E. Whitten, J. W. Soares, A. M. Meehan, D. M. Steeves, *Nanophotonic Mater.* **2008**, *7030*, 106.

[59] T. Heinrich, C. H.-H. Traulsen, E. Darlatt, S. Richter, J. Poppenberg, N. L. Traulsen, I. Linder, A. Lippitz, P. M. Dietrich, B. Dib, W. E. S. Unger, C. A. Schalley, *RSC Adv.* **2014**, *4*, 17694.

[60] D. G. Castner, K. Hinds, D. W. Grainger, *Langmuir* **1996**, *12*, 5083.

[61] J. Dvorak, T. Jirsak, J. A. Rodriguez, *Surf. Sci.* **2001**, *479*, 155.

[62] A. G. Shard, *J. Vac. Sci. Technol., A* **2020**, *38*, 041201.

[63] L. G. Mar, P. Y. Timbrell, R. N. Lamb, *Thin Solid Films* **1993**, *223*, 341.

[64] A. G. Marrani, F. Caprioli, A. Boccia, R. Zanoni, F. Decker, *J. Solid State Electrochem.* **2014**, *18*, 505.

[65] X. Q. Wei, B. Y. Man, M. Liu, C. S. Xue, H. Z. Zhuang, C. Yang, *Phys. B* **2007**, *388*, 145.

[66] A. Drici, G. Djeteli, G. Tchangbedji, H. Derouiche, K. Jondo, K. Napo, J. C. Bernède, S. Ouro-Djobo, M. Gbagba, *Phys. Status Solidi A* **2004**, *201*, 1528.

[67] Y. Wang, J. Im, J. W. Soares, D. M. Steeves, J. E. Whitten, *Langmuir* **2016**, *32*, 3848.

[68] J. F. Watts, J. Wolstenholme, in *An Introduction to Surface Analysis by XPS and AES*, 2nd ed., John Wiley & Sons, Hoboken, NJ **2019**, p. 97.

[69] C. Ton-That, A. G. Shard, R. H. Bradley, *Langmuir* **2000**, *16*, 2281.

[70] P. J. Cumpson, *J. Electron Spectrosc. Relat. Phenom.* **1995**, *73*, 25.

[71] B. Halevi, J. M. Vohs, *Catal. Lett.* **2006**, *111*, 1.

[72] F. Vurpillot, C. Oberdorfer, *Ultramicroscopy* **2015**, *159*, 202.

[73] J. R. Boes, O. Mamun, K. Winther, T. Bligaard, *J. Phys. Chem. A* **2019**, *123*, 2281.

[74] A. Kornherr, S. Hansal, W. E. G. Hansal, G. E. Nauer, G. Zifferer, *Macromol. Symp.* **2004**, *217*, 295.

[75] A. Kornherr, S. A. French, A. A. Sokol, C. R. A. Catlow, S. Hansal, W. E. G. Hansal, J. O. Besenhard, H. Kronberger, G. E. Nauer, G. Zifferer, *Chem. Phys. Lett.* **2004**, *393*, 107.

[76] A. Jablonski, C. J. Powell, *NIST Electron Inelastic-Mean-Free-Path Database – Version 1.2*, National Institute of Standards and Technology, Gaithersburg, MD **2010**.

[77] L. M. Bishop, J. C. Yeager, X. Chen, J. N. Wheeler, M. D. Torelli, M. C. Benson, S. D. Burke, J. A. Pedersen, R. J. Hamers, *Langmuir* **2012**, *28*, 1322.

[78] J. Lieto, M. Wolf, B. A. Matrana, M. Prochazka, B. Tesche, H. Knoezinger, B. C. Gates, *J. Phys. Chem.* **1985**, *89*, 991.

[79] M. Kirchhof, K. Gugeler, F. R. Fischer, M. Nowakowski, A. Bauer, S. Alvarez-Barcia, K. Abitaev, M. Schnierle, Y. Qawasmi, W. Frey, A. Baro, D. P. Estes, T. Sottmann, M. R. Ringenberg, B. Plietker, M. Bauer, J. Kästner, S. Laschat, *Organometallics* **2020**, *39*, 3131.

[80] H.-H. Nguyen, Z. Li, T. Enenkel, J. Hildebrand, M. Bauer, M. Dyballa, D. P. Estes, *J. Phys. Chem. C* **2021**, *125*, 14627.